TIME-DOMAIN NUMERICAL MODELING OF WAVE PROPAGATION IN POROELASTIC MEDIA WITH RATIONAL APPROXIMATION OF THE FRACTIONAL ATTENUATION

JIANGMING XIE, MAOJUN LI, AND MIAO-JUNG YVONNE OU

Dedicated to our friend and colleague Robert P. Gilbert on the occasion of his 90th birthday

Abstract. In this work, we investigate the poroelastic waves by solving the time-domain Biot-JKD equation with an efficient numerical method. The viscous dissipation occurring in the pores depends on the square root of the frequency and is described by the Johnson-Koplik-Dashen (JKD) dynamic tortuosity/permeability model. The temporal convolutions of order 1/2 shifted fractional derivatives are involved in the time-domain Biot-JKD model, causing the problem to be stiff and challenging to be implemented numerically. Based on the best relative approximation of the square-root function, we design an efficient algorithm to approximate and localize the convolution kernel by introducing a finite number of auxiliary variables that satisfy a local system of ordinary differential equations. The imperfect hydraulic contact condition is used to describe the interface boundary conditions and the Runge-Kutta discontinuous Galerkin (RKDG) method together with the splitting method is applied to compute the numerical solutions. Several numerical examples are presented to show the accuracy and efficiency of our approach.

Keyword: poroelastic media, Biot-JKD model, temporal convolution, stiff system, Chebyshev approximation, splitting method, RKDG method.

1. Introduction

Porous media consist of a solid matrix saturated with fluids that can flow through the pores freely and has important applications in petroleum rocks, engineering composites, energy conversion and energy storage. The propagation of waves in these media can be described by poroelasticity theory, which was originally developed by Biot (2; 3; 4). Biot theory predicts that there are three waves propagating in isotropic poroelastic materials. In the order of decreasing wave speeds, they are classified as: *fast p wave*, which are analogous to the standard elastic *p wave*; *s wave*, which are analogous to the elastic *shear wave*; and *slow p wave*, which exhibits substantial phase difference between the solid matrix and fluid. Because of the viscous effect, the *fast p wave* and *s wave* are lightly damped, while the *slow p wave* is strongly damped. Simultaneously, the viscous dissipation also causes slight dispersion in the *fast p wave* and *s wave* and strong dispersion in the *slow p wave*.

In Biot's theory, two frequency regimes of the low-frequency range (LF) and the high-frequency range (HF) are separated by the critical frequency f_c. In the LF regime, the fluid inside the pores is assumed to be of Poiseuille type, making the viscous effect proportional to the relative velocity between pore fluid and the solid matrix. In the HF regime, the viscous effect depends on the square root of the frequency, resulting in a convolution term in the time-domain. In (3), Biot firstly presented an expression of the memory kernel for particular geometries. In (18), Johnson-Koplik-Dashen (JKD) derived a more general model of dynamic permeability, which accounted for the viscous effects in a full frequency range and was in agreement with Biot's theory for the low frequency regime. In (1), Avellaneda and Torquato pointed out that the permeability in the frequency domain can be represented as a Stieltjes integral with a probability measure; mathematically, this is by far the most general theory for the high-frequency correction of Biot's LF equations. In (26), Pride et al. developed a drag force model for more general pore geometry by adding correction to the JKD model when the cross-section size of pore space varies significantly along the fluid trajectory.

Date: December 9, 2021.

In the LF regime, the major difficultly for numerical simulation is to handle the stiffness of the Biot equations; see (20; 12; 29; 27; 5; 15; 16; 33; 32; 11) for reference. In the HF regime, not only the viscous term but also the temporal convolution is hard to implement numerically, complicating the modeling task greatly. Two approaches have appeared in the literature to approximate the Biot-JKD equations directly in the time-domain. The first one is to discretize the convolution term directly by defining a time convolution product (23). The second one is to approximate the memory kernel by the summation of exponentials and replace the temporal convolution by the auxiliary variables satisfying local differential equations. In (10), the Fourier transform of the memory kernel (dynamic tortuosity) is approximated by a sum of Zener kernels in the frequency domain. In (22), the Biot-DA (diffusive approximation) model with the Gauss-Laguerre quadrature formula is developed to approximate the Biot-JKD model, which is based on the diffusive representation of the fractional derivative. Instead of the Gauss-Laguerre quadrature, a linear optimization procedure has been used to determine the coefficients of the DA model (6; 7), which is more accurate than the Gauss-Laguerre formula. Furthermore, a nonlinear optimization method is developed in (8) to improve the performances of the linear optimization method. In (24; 25; 31), based on the fact that the dynamic tortuosity in the Laplace domain, including the JKD model, can be exactly represented with a Stieltjes function, whose two-sided residue approximation is used to approximate the tortuosity. This approach is more accurate than the optimization method.

Both the optimization method and the Stieltjes function approach work well for the approximation of the convolution kernel. However, although the Stieltjes function approach has high accuracy, it involves solving a linear system with very large condition number. The linear optimization method also encounter a high condition number linear system. Besides, both methods are sensitive to the choice of sample points and an improper choice of the nodes may lead to lower convergence, especially for the linear optimization method. To avoid solving a system of high condition number, a more general method of the best relative Chebyshev approximation for the square root functions (9; 30) is developed in this work. One of the advantage is that it can be implemented easily without the need of forming the system or choosing the interpolation points.

The objective of this paper is to develop an efficient algorithm to simulate wave propagation in orthotropic poroelastic media. For this purpose, we apply the Runge-Kutta discontinuous Galerkin (RKDG) method to solve the Biot-JKD equations. Due to the existence of the temporal convolution, a naive implementation will be very expensive and highly inefficient. To overcome this difficulty, we design a fast algorithm by utilizing **the best relative Chebyshev approximation of the square-root function** appearing in the JKD model. The main idea is to approximate the JKD dynamic tortuosity in the Laplace domain by rational functions, and then apply the inverse Laplace transform to obtain the time-domain approximation of the convolution. By this approach, the temporal convolution is replaced by a set of local ODEs with auxiliary variables, and thus a fast evaluation is straightforward. In addition, the viscous dissipation is challenging to be implemented since the viscous term has its own intrinsic timescale, which is independent of the mesh grids and may cause the poroelasticity system to be stiff. To tackle this, we apply the second-order Strang splitting method to deal with the viscous term by splitting the Biot-JKD equations into a homogeneous hyperbolic system and a system of ordinary differential equations (ODEs). The imperfect hydraulic contact condition is use to handle the interface conditions when heterogeneous poroelastic media is considered. We give a complete dispersion and energy analysis of the Biot-JKD model.

The remainder of this paper is organized as follows. In Section 2, the mathematical formulation of the governing equations is described. In Section 3, we present the dispersion analysis. In Section 4, we introduce the fast algorithm based on the best relative Chebyshev approximation of the square-root function. A brief description of the numerical method is in Section 5. Finally, several numerical tests are provided in Section 6.

2. Mathematical model for wave propagation in transversely isotropic poroelastic media

Let $\mathbf{u}$ be the skeleton solid displacement vector, $\mathbf{U}$ the fluid displacement vector, $\mathbf{w} := \phi(\mathbf{U} - \mathbf{u})$ the relative motion of the fluid scaled by the porosity ϕ and $\zeta := -\nabla \cdot \mathbf{w}$ the variation in fluid content. The

solid velocity $\mathbf{v}$ and the relative fluid velocity $\mathbf{q}$ are defined by

$$\mathbf{v} := \frac{\partial \mathbf{u}}{\partial t}, \quad \mathbf{q} := \frac{\partial \mathbf{w}}{\partial t}. \tag{2.1}$$

2.1. **The constitutive relation.** Let the z axis be the symmetry axis, the stress-strain relations for a transversely isotropic elastic material has the following form:

$$\boldsymbol{\tau} = \mathbf{C}\boldsymbol{\epsilon}, \tag{2.2}$$

where the matrix elastic stiffness tensor $\mathbf{C}$, stress tensor $\boldsymbol{\tau}$, and strain tensor $\boldsymbol{\epsilon}$ are defined as

$$\mathbf{C} = \begin{pmatrix} c_{11} & c_{13} & 0 \\ c_{13} & c_{33} & 0 \\ 0 & 0 & c_{55} \end{pmatrix}, \quad \boldsymbol{\tau} = (\tau_{11}\ \tau_{33}\ \tau_{13})^T, \quad \boldsymbol{\epsilon} = (\epsilon_{11}\ \epsilon_{33}\ 2\epsilon_{13}\ )^T, \tag{2.3}$$

with $\epsilon_{ij} = \frac{1}{2}(\partial_i u_j + \partial_j u_i)$. Here and hereafter, the subscripts 1 and 3 represent the x and z axes, respectively. The constitutive relations are expressed as

$$\boldsymbol{\tau} = \mathbf{C}\boldsymbol{\epsilon} - \boldsymbol{\beta} p = \mathbf{C}^u\boldsymbol{\epsilon} - M\boldsymbol{\beta}\zeta, \tag{2.4}$$

$$p = M\left(\zeta - \boldsymbol{\beta}^T\boldsymbol{\epsilon}\right), \tag{2.5}$$

where $\mathbf{C}^u$ is the undrained matrix elasticity tensor and is determined by

$$\begin{aligned} \mathbf{C}^u : &= \mathbf{C} + M\boldsymbol{\beta}\boldsymbol{\beta}^T, \quad \boldsymbol{\beta} := (\beta_1,\ \beta_3,\ 0)^T, \\ \beta_1 : &= 1 - \frac{c_{11}+c_{12}+c_{13}}{3K_s}, \quad \beta_3 := 1 - \frac{2c_{13}+c_{33}}{3K_s}, \\ M : &= \frac{K_s^2}{K_s\left[1+\phi(K_s/K_f-1)\right] - \left(2c_{11}+c_{33}+2c_{12}+4c_{13}\right)/9}, \end{aligned}$$

with K_s and K_f being the bulk modulus of the skeleton and pore fluid, respectively.

2.2. **Equations of motion.** The equations of motion are given by the conservation of momentum as

$$\rho\frac{\partial \mathbf{v}}{\partial t} + \rho_f\frac{\partial \mathbf{q}}{\partial t} = \nabla\cdot\overline{\boldsymbol{\tau}}, \tag{2.6}$$

where ρ_s is the density of constituent solid, $\rho = (1-\phi)\rho_s + \phi\rho_f$ the bulk density of the medium and $\overline{\boldsymbol{\tau}} = \begin{bmatrix} \tau_{11} & \tau_{13} \\ \tau_{13} & \tau_{33} \end{bmatrix}$ with $\nabla\cdot\overline{\boldsymbol{\tau}} = (\partial_x\tau_{11} + \partial_z\tau_{13},\ \partial_x\tau_{13} + \partial_z\tau_{33})^T$.

The generalized Darcy's law is

$$\rho_f\frac{\partial \mathbf{v}}{\partial t} + \mathrm{diag}\left(\frac{\rho_f}{\phi}\right)\check{\boldsymbol{\alpha}} * \frac{\partial \mathbf{q}}{\partial t} = -\nabla p, \tag{2.7}$$

where $*$ denotes the temporal convolution and $\check{\boldsymbol{\alpha}} = (\check{\alpha}_1, \check{\alpha}_3)^T$ is the inverse Laplace transform of the dynamic tortuosity $\boldsymbol{\alpha}(s)$ with $s = \mathrm{i}\omega, \mathrm{i} = \sqrt{-1}$ and ω is the frequency.

2.3. **The Biot-JKD equation.** In the LF regime, the viscous effect is proportional to the relative velocity between pore fluid and the solid matrix, which leads to

$$\check{\alpha}_j(t) = \alpha_{\infty j}\delta(t) + \frac{\eta\phi}{\kappa_j\rho_f}H(t),\ j = 1, 3, \tag{2.8}$$

where $\delta(t)$ is the Dirac function and $H(t)$ the Heaviside function. In the HF regime, the viscous effect depends on the square root of the frequency, resulting in a memory kernel in time-domain. The JKD model (18) in the frequency domain is

$$\alpha_j(s) := \alpha_{\infty j} + \frac{\eta\phi}{s\kappa_j\rho_f}\left(1 + s\frac{4\alpha_{\infty j}^2\kappa_j^2\rho_f}{\eta\Lambda_j^2\phi^2}\right)^{\frac{1}{2}},\ j = 1, 3,$$

where $\Lambda_j = \sqrt{\frac{4\alpha_{\infty j}\kappa_j}{\phi \mathrm{P}_j}}$ is the viscous characteristic length and P_j is the Pride number. Set

$$\lambda_j = \frac{\eta\phi^2\Lambda_j^2}{4\alpha_{\infty j}^2\kappa_j^2\rho_f},\ j=1,3, \tag{2.9}$$

then we have

$$\alpha_j(s) := \alpha_{\infty j} + \frac{\eta\phi}{s\kappa_j\rho_f\sqrt{\lambda_j}}\left(s+\lambda_j\right)^{\frac{1}{2}},\ j=1,3. \tag{2.10}$$

Combining (2.7) and (2.10), we obtain the Darcy's law in the time-domain

$$\rho_f\frac{\partial \mathbf{v}}{\partial t} + \mathrm{diag}\left(\frac{\alpha_{\infty j}\rho_f}{\phi}\right)\frac{\partial \mathbf{q}}{\partial t} + \nabla p = -\mathrm{diag}\left(\frac{\eta}{\kappa_j\sqrt{\lambda_j}}\left(\partial_t+\lambda_j\right)^{1/2}\right)\mathbf{q},\ j=1,3. \tag{2.11}$$

Taking derivative on both sides (2.4) and (2.5) with respect to time t, and combining the motion equation (2.6), we rewrite the Biot-JKD equation as

$$\frac{\partial \boldsymbol{\tau}}{\partial t} = \frac{\partial}{\partial t}\left(\mathbf{C}^u\boldsymbol{\epsilon} - M\boldsymbol{\beta}\zeta\right), \tag{2.12}$$

$$\frac{\partial p}{\partial t} = \frac{\partial}{\partial t}\left(M\left(\zeta - \boldsymbol{\beta}^T\boldsymbol{\epsilon}\right)\right), \tag{2.13}$$

$$\rho\frac{\partial \mathbf{v}}{\partial t} + \rho_f\frac{\partial \mathbf{q}}{\partial t} = \nabla\cdot\overline{\boldsymbol{\tau}}, \tag{2.14}$$

$$\rho_f\frac{\partial \mathbf{v}}{\partial t} + \mathrm{diag}\left(\frac{\alpha_{\infty j}\rho_f}{\phi}\right)\frac{\partial \mathbf{q}}{\partial t} + \nabla p = -\mathrm{diag}\left(\vartheta_j\left(\partial_t+\lambda_j\right)^{1/2}\right)\mathbf{q},\ j=1,3, \tag{2.15}$$

where $(\partial_t+\lambda_j)^{1/2}$ is the Caputo fractional derivative with the shifted factor λ_j and $\vartheta_j = \frac{\eta}{\kappa_j\sqrt{\lambda_j}}$. Based on the diffusive representation of the fractional derivative, we have

$$\left(\partial_t+\lambda_j\right)^{1/2} q_j = e^{-\lambda_j t}\partial_t^{1/2}\left(e^{\lambda_j t}q_j\right) = \frac{2}{\pi}\int_0^\infty \psi_j(y,t)dy,\ j=1,3, \tag{2.16}$$

where the auxiliary variables are defined as

$$\psi_j(y,t) = \int_0^t e^{-(y^2+\lambda_j)(t-\tau)}\left[\lambda_j q_j(\tau) + \partial_\tau q_j(\tau)\right]d\tau.$$

It is easy to check that the auxiliary variables satisfy the following equations

$$\frac{\partial \psi_j}{\partial t} = -\left(y^2+\lambda_j\right)\psi_j + \left[\lambda_j q_j + \partial_t q_j\right],\ j=1,3, \tag{2.17}$$

with zero initial conditions.

Theorem 2.1. *(energy decay) Consider the Biot-JKD model (2.12)-(2.15) without force. Define*

$$\begin{aligned}
\mathcal{E}_1 &= \frac{1}{2}\int_{\mathbb{R}^2}\left((v_1,\ q_1)\mathcal{M}_1(v_1,\ q_1)^T + (v_3,\ q_3)\mathcal{M}_3(v_3,\ q_3)^T\right)dxdz,\\
\mathcal{E}_2 &= \frac{1}{2}\int_{\mathbb{R}^2}\left((\boldsymbol{\tau}+p\boldsymbol{\beta})^T\boldsymbol{C}^{-1}(\boldsymbol{\tau}+p\boldsymbol{\beta}) + \frac{1}{M}p^2\right)dxdz,\\
\mathcal{E}_3 &= \frac{1}{\pi}\int_{\mathbb{R}^2}\int_0^\infty(\boldsymbol{\psi}-\mathbf{q})^T\, diag\left(\frac{\vartheta_j}{y^2+2\lambda_j}\right)(\boldsymbol{\psi}-\mathbf{q})dxdz,
\end{aligned}$$

with $\mathcal{M}_j = \begin{bmatrix}\rho & \rho_f\\ \rho_f & \mu_j\end{bmatrix}$, $\mu_j = \frac{\alpha_{\infty j}\rho_f}{\phi}$ *and* $\boldsymbol{\psi} = (\psi_1,\psi_3)^T$, *then*

$$\mathcal{E} = \mathcal{E}_1 + \mathcal{E}_2 + \mathcal{E}_3,$$

is the total energy, which satisfies

$$\frac{d\mathcal{E}}{dt} = -\frac{2}{\pi}\int_{\mathbb{R}^2}\int_0^\infty\left[\boldsymbol{\psi}^T\, diag\left(\frac{y^2+\lambda_j}{y^2+2\lambda_j}\vartheta_j\right)\boldsymbol{\psi} + \mathbf{q}^T\, diag\left(\frac{\lambda_j\vartheta_j}{y^2+2\lambda_j}\right)\mathbf{q}\right]dydxdz < 0,\ j=1,3. \tag{2.18}$$

Proof. We refer the readers to A for the proof. □

2.4. **The approximate Biot-JKD equation.** The Biot-JKD model (2.12)-(2.15) is hard to be implemented due to the existence of the temporal convolution. To overcome this difficulty, we derive an approximated Biot-JKD model by utilizing the best relative Chebyshev approximation of the square-root function (9; 30)

$$\sqrt{s} \backsimeq -\sum_{k=1}^{m} \frac{\omega_k}{s+p_k} + \omega_{m+1} s + \omega_{m+2} := \Phi(s), \tag{2.19}$$

where $p_k > 0$ and $\omega_k > 0$ are the poles and weights respectively. Consequently, we have

$$(s+\lambda_j)^{\frac{1}{2}} \backsimeq -\sum_{k=1}^{m} \frac{\omega_k^j}{s+\lambda_j+p_k^j} + \omega_{m+1}^j (s+\lambda_j) + \omega_{m+2}^j := \Phi(s+\lambda_j),\ j=1,3. \tag{2.20}$$

With the above approximation, the Darcy's law (2.15) in the Laplace domain can be expressed as

$$\rho_f (s\hat{\mathbf{v}}) + \mathrm{diag}\,(\mu_j)\,(s\hat{\mathbf{q}}) + \nabla \hat{p} + \mathrm{diag}\left(\vartheta_j \left(-\sum_{k=1}^{m} \frac{\omega_k^j}{s+\lambda_j+p_k^j} + \omega_{m+1}^j (s+\lambda_j) + \omega_{m+2}^j\right)\right) \hat{\mathbf{q}} = 0. \tag{2.21}$$

Define the auxiliary variables

$$\hat{\mathbf{H}}_k = \mathrm{diag}\left(\frac{1}{s+\lambda_j+p_k^j}\right) \hat{\mathbf{q}},\ j=1,3. \tag{2.22}$$

By applying the inverse Laplace transform, we obtain

$$\begin{aligned} &\rho_f \frac{\partial \mathbf{v}}{\partial t} + \mathrm{diag}\left(\mu_j + \vartheta_j \omega_{m+1}^j\right) \frac{\partial \mathbf{q}}{\partial t} + \nabla p \\ &= \sum_{k=1}^{m} \mathrm{diag}\left(\vartheta_j \omega_k^j\right) \mathbf{H}_k - \mathrm{diag}\left(\vartheta_j \left(\omega_{m+1}^j \lambda_j + \omega_{m+2}^j\right)\right) \mathbf{q}, \end{aligned} \tag{2.23}$$

where zero initial conditions for $\mathbf{q}$ are used. According to (2.22), we have

$$\frac{\partial H_k^j}{\partial t} = -\left(p_k^j + \lambda_j\right) H_k^j + q_j, \quad H_k^j|_{t=0} = 0, \quad k = 1, \cdots m,\ j=1,3. \tag{2.24}$$

From (2.14) and (2.23), we derive

$$\frac{\partial q_1}{\partial t} + \frac{\rho_f}{\gamma_1}\left(\frac{\partial \tau_{11}}{\partial x} + \frac{\partial \tau_{13}}{\partial z}\right) + \frac{\rho}{\gamma_1}\frac{\partial p}{\partial x} = \frac{\rho \vartheta_1}{\gamma_1}\left[\sum_{k=1}^{m} \omega_k^1 H_k^1 - \left(\omega_{m+1}^1 \lambda_1 + \omega_{m+2}^1\right) q_1\right], \tag{2.25}$$

$$\frac{\partial q_3}{\partial t} + \frac{\rho_f}{\gamma_3}\left(\frac{\partial \tau_{13}}{\partial x} + \frac{\partial \tau_{33}}{\partial z}\right) + \frac{\rho}{\gamma_3}\frac{\partial p}{\partial z} = \frac{\rho \vartheta_3}{\gamma_3}\left[\sum_{k=1}^{m} \omega_k^3 H_k^3 - \left(\omega_{m+1}^3 \lambda_3 + \omega_{m+2}^3\right) q_3\right], \tag{2.26}$$

$$\frac{\partial v_1}{\partial t} - \frac{\mu_1 + \vartheta_1 \omega_{m+1}^1}{\gamma_1}\left(\frac{\partial \tau_{11}}{\partial x} - \frac{\partial \tau_{13}}{\partial z}\right) - \frac{\rho_f}{\gamma_1}\frac{\partial p}{\partial x} = \frac{\rho_f \vartheta_1}{\gamma_1}\left[-\sum_{k=1}^{m} \omega_k^1 H_k^1 + \left(\omega_{m+1}^1 \lambda_1 + \omega_{m+2}^1\right) q_1\right], \tag{2.27}$$

$$\frac{\partial v_3}{\partial t} - \frac{\mu_3 + \vartheta_3 \omega_{m+1}^3}{\gamma_3}\left(\frac{\partial \tau_{13}}{\partial x} + \frac{\partial \tau_{33}}{\partial z}\right) - \frac{\rho_f}{\gamma_3}\frac{\partial p}{\partial z} = \frac{\rho_f \vartheta_3}{\gamma_3}\left[-\sum_{k=1}^{m} \omega_k^3 H_k^3 + \left(\omega_{m+1}^3 \lambda_3 + \omega_{m+2}^3\right) q_3\right], \tag{2.28}$$

where $\gamma_j = \rho\mu_j - \rho_f^2 + \rho\vartheta_j \omega_{m+1}^j, j = 1,3$. Simultaneously, by (2.12), we have

$$\partial_t \tau_{11} = c_{11}^u \partial_x v_1 + c_{13}^u \partial_z v_3 + \beta_1 M(\partial_x q_1 + \partial_z q_3), \tag{2.29}$$

$$\partial_t \tau_{33} = c_{13}^u \partial_x v_1 + c_{33}^u \partial_z v_3 + \beta_3 M(\partial_x q_1 + \partial_z q_3), \tag{2.30}$$

$$\partial_t \tau_{13} = c_{55}^u (\partial_z v_1 + \partial_x v_3), \tag{2.31}$$

$$\partial_t p = -\beta_1 M \partial_x v_1 - \beta_3 M \partial_z v_3 - M(\partial_x q_1 + \partial_z q_3). \tag{2.32}$$

In terms of the unknown vector $\mathbf{Q} = \left(\tau_{11},\ \tau_{33},\ \tau_{13},\ p,\ v_1,\ v_3,\ q_1,\ q_3,\ H_1^1, \cdots, H_m^1,\ H_1^3, \cdots, H_m^3\right)^T$ and the external source $\mathbf{S} = (s_{11},\ s_{33},\ s_{13},\ 0,\ 0,\ s_f,\ 0,\ 0,\ 0_1, \cdots, 0_m,\ 0_1, \cdots, 0_m)^T$, the first-order governing system (2.25)-(2.32) reads as

$$\frac{\partial \mathbf{Q}}{\partial t} + \mathbf{A}\frac{\partial \mathbf{Q}}{\partial x} + \mathbf{B}\frac{\partial \mathbf{Q}}{\partial z} = \mathbf{H}\mathbf{Q} + \mathbf{S}, \tag{2.33}$$

where

$$\mathbf{A} = \begin{bmatrix} \mathbf{A}_1 & \mathbf{0} \\ \mathbf{0} & \mathbf{0} \end{bmatrix},\ \mathbf{B} = \begin{bmatrix} \mathbf{B}_1 & \mathbf{0} \\ \mathbf{0} & \mathbf{0} \end{bmatrix},\ \mathbf{H} = \begin{bmatrix} \mathbf{H}_1 & \mathbf{H}_2 \\ \mathbf{H}_4 & \mathbf{H}_3 \end{bmatrix}, \tag{2.34}$$

and

$$\mathbf{A}_1 = -\begin{bmatrix} 0 & 0 & 0 & 0 & c_{11}^u & 0 & \beta_1 M & 0 \\ 0 & 0 & 0 & 0 & c_{13}^u & 0 & \beta_3 M & 0 \\ 0 & 0 & 0 & 0 & 0 & c_{55}^u & 0 & 0 \\ 0 & 0 & 0 & 0 & -\beta_1 M & 0 & -M & 0 \\ \frac{\mu_1+\vartheta_1\omega_{m+1}^1}{\gamma_1} & 0 & 0 & \frac{\rho_f}{\gamma_1} & 0 & 0 & 0 & 0 \\ 0 & 0 & \frac{\mu_3+\vartheta_3\omega_{m+1}^3}{\gamma_3} & 0 & 0 & 0 & 0 & 0 \\ -\frac{\rho_f}{\gamma_1} & 0 & 0 & -\frac{\rho}{\gamma_1} & 0 & 0 & 0 & 0 \\ 0 & 0 & -\frac{\rho_f}{\gamma_3} & 0 & 0 & 0 & 0 & 0 \end{bmatrix},$$

$$\mathbf{B}_1 = -\begin{bmatrix} 0 & 0 & 0 & 0 & 0 & c_{13}^u & 0 & \beta_1 M \\ 0 & 0 & 0 & 0 & 0 & c_{33}^u & 0 & \beta_3 M \\ 0 & 0 & 0 & 0 & c_{55}^u & 0 & 0 & 0 \\ 0 & 0 & 0 & 0 & 0 & -\beta_3 M & 0 & -M \\ 0 & 0 & \frac{\mu_1+\vartheta_1\omega_{m+1}^1}{\gamma_1} & 0 & 0 & 0 & 0 & 0 \\ 0 & \frac{\mu_3+\vartheta_3\omega_{m+1}^3}{\gamma_3} & 0 & \frac{\rho_f}{\gamma_3} & 0 & 0 & 0 & 0 \\ 0 & 0 & -\frac{\rho_f}{\gamma_1} & 0 & 0 & 0 & 0 & 0 \\ 0 & -\frac{\rho_f}{\gamma_3} & 0 & -\frac{\rho}{\gamma_3} & 0 & 0 & 0 & 0 \end{bmatrix},$$

$$\mathbf{H}_1 = \begin{bmatrix} 0&0&0&0&0&0&0&0\\ 0&0&0&0&0&0&0&0\\ 0&0&0&0&0&0&0&0\\ 0&0&0&0&0&0&0&0\\ 0&0&0&0&0&0&\frac{\rho_f\vartheta_1\left(\lambda_1\omega^1_{m+1}+\omega^1_{m+2}\right)}{\gamma_1}&0\\ 0&0&0&0&0&0&0&\frac{\rho_f\vartheta_3\left(\lambda_3\omega^3_{m+1}+\omega^3_{m+2}\right)}{\gamma_3}\\ 0&0&0&0&0&0&-\frac{\rho\vartheta_1\left(\lambda_1\omega^1_{m+1}+\omega^1_{m+2}\right)}{\gamma_1}&0\\ 0&0&0&0&0&0&0&-\frac{\rho\vartheta_3\left(\lambda_3\omega^3_{m+1}+\omega^3_{m+2}\right)}{\gamma_3} \end{bmatrix},$$

$$\mathbf{H}_2 = \begin{bmatrix} 0&0&\cdots&0&0&0&\cdots&0\\ 0&0&\cdots&0&0&0&\cdots&0\\ 0&0&\cdots&0&0&0&\cdots&0\\ 0&0&\cdots&0&0&0&\cdots&0\\ -\frac{\rho_f\vartheta_1\omega^1_1}{\gamma_1}&-\frac{\rho_f\vartheta_1\omega^1_2}{\gamma_1}&\cdots&-\frac{\rho_f\vartheta_1\omega^1_m}{\gamma_1}&0&0&\cdots&0\\ 0&0&\cdots&0&-\frac{\rho_f\vartheta_3\omega^3_1}{\gamma_3}&-\frac{\rho_f\vartheta_3\omega^3_2}{\gamma_3}&\cdots&-\frac{\rho_f\vartheta_3\omega^3_m}{\gamma_3}\\ \frac{\rho\vartheta_1\omega^1_1}{\gamma_1}&\frac{\rho\vartheta_1\omega^1_2}{\gamma_1}&\cdots&\frac{\rho\vartheta_1\omega^1_m}{\gamma_1}&0&0&\cdots&0\\ 0&0&\cdots&0&\frac{\rho\vartheta_3\omega^3_1}{\gamma_3}&\frac{\rho\vartheta_3\omega^3_2}{\gamma_3}&\cdots&\frac{\rho\vartheta_3\omega^3_m}{\gamma_3} \end{bmatrix},$$

$$\mathbf{H}_4 = \begin{bmatrix} 0&0&0&0&0&0&1&0\\ 0&0&0&0&0&0&1&0\\ \vdots&\vdots&\vdots&\vdots&\vdots&\vdots&\vdots&\vdots\\ 0&0&0&0&0&0&1&0\\ 0&0&0&0&0&0&0&1\\ 0&0&0&0&0&0&0&1\\ \vdots&\vdots&\vdots&\vdots&\vdots&\vdots&\vdots&\vdots\\ 0&0&0&0&0&0&0&1 \end{bmatrix}, \quad \mathbf{H}_3 = \begin{bmatrix} -\mathrm{diag}\left(p^1_k+\lambda_1\right) & \mathbf{0}\\ \mathbf{0} & -\mathrm{diag}\left(p^3_k+\lambda_3\right) \end{bmatrix}.$$

It is this system (2.33) with $2m+8$ unknowns that forms the basis for our numerical work, in which the temporal convolution in (2.15) is divided into a series of local ordinary differential equations with finite memories. The dimension of this system increases linearly with the number of auxiliary variables. Note that the flux of the auxiliary variables H^j_k is exactly zero, making the system very simple to implement .

Theorem 2.2. *(eigenvalues of* $\mathbf{H}$*) Suppose* $\{p^j_k\}_{k=1}^m$ *is an increasing sequence w.r.t.* k *for each fixed* $j = 1, 3$*, then zero is an eigenvalue of* $\mathbf{H}$ *with multiplicity 6, and the* $2m+2$ *nonzero eigenvalues* $\{\tilde{\lambda}^j_k\}_{k=1}^{m+1}, j = 1, 3$ *satisfy*

$$0 < \tilde{\lambda}^j_1 < p^j_1 + \lambda^j_1 < \cdots < \tilde{\lambda}^j_m < p^j_m + \lambda_j < \tilde{\lambda}^j_{m+1},\ j = 1, 3.$$

Proof. We refer the readers to B for the proof. □

3. Dispersion analysis

In this section, we present the dispersion analysis of (2.33), where the phase velocities and the attenuation will be deduced. Assume that the particle velocity and stress have the plane wave form

$$\begin{aligned} \mathbf{V} = (v_x,\ v_z,\ q_x,\ q_z)^T &= \mathbf{V}_0 \exp(\mathrm{i}(\omega t - k_x x - k_z z)),\\ \mathbf{T} = (\tau_{xx},\ \tau_{zz},\ \tau_{xz},\ -p)^T &= \mathbf{T}_0 \exp(\mathrm{i}(\omega t - k_x x - k_z z)), \end{aligned}$$

where $\mathbf{V}_0,\ \mathbf{T}_0$ are constant vectors, ω is the angular frequency, and $\vec{k} = (k_x,\ k_z) = k\,(l_x,\ l_z)$ is the wave vector with k being the wave number and $(l_x,\ l_z)$ being the unit wave direction. Injecting the plane wave to the stress-strain equations (2.29)-(2.32) gives

$$\omega \mathbf{T}_0 = -k\mathbf{F}\mathbf{V}_0, \tag{3.1}$$

where $\mathbf{F}$ is given by

$$\mathbf{F} = \begin{bmatrix} l_x c_{11}^u & l_z c_{13}^u & \beta_1 M l_x & \beta_1 M l_z \\ l_x c_{13}^u & l_z c_{33}^u & \beta_3 M l_x & \beta_3 M l_z \\ l_z c_{55}^u & l_x c_{55}^u & 0 & 0 \\ \beta_1 M l_x & \beta_3 M l_z & M l_x & M l_z \end{bmatrix}.$$

Substituting the plane wave to the equations of motion (2.25)-(2.28) gives

$$-k\mathbf{L}\mathbf{T}_0 = \omega\boldsymbol{\Gamma}\mathbf{V}_0, \tag{3.2}$$

where $\boldsymbol{\Gamma}$ and $\mathbf{L}$ are given by

$$\mathbf{L} = \begin{bmatrix} l_x & 0 & l_z & 0 \\ 0 & l_z & l_x & 0 \\ 0 & 0 & 0 & l_x \\ 0 & 0 & 0 & l_z \end{bmatrix}, \quad \boldsymbol{\Gamma} = \begin{bmatrix} \rho & 0 & \rho_f & 0 \\ 0 & \rho & 0 & \rho_f \\ \rho_f & 0 & \frac{Y_1(\omega)}{\mathrm{i}\omega} & 0 \\ 0 & \rho_f & 0 & \frac{Y_3(\omega)}{\mathrm{i}\omega} \end{bmatrix},$$

with

$$Y_j(\omega) = \mathrm{i}\omega\mu_j + \frac{\eta}{\kappa_j\sqrt{\lambda_j}}\left[-\sum_{k=1}^{m}\frac{\omega_k^j}{\mathrm{i}\omega+\lambda_j+p_k^j} + \omega_{m+1}^j(\mathrm{i}\omega+\lambda_j) + \omega_{m+2}^j\right],\ j=1,3.$$

For the LF Biot equation, we have

$$Y_j(\omega) := \mathrm{i}\omega\mu_j + \frac{\eta}{\kappa_j},\ j=1,\ 3,$$

while for the Biot-JKD equation, we have

$$Y_j(\omega) = \mathrm{i}\omega\mu_j + \frac{\eta}{\kappa_j\sqrt{\lambda_j}}\left(\mathrm{i}\omega+\lambda_j\right)^{\frac{1}{2}},\ j=1,3.$$

Together (3.1) and (3.2) lead to

$$\boldsymbol{\Gamma}^{-1}\mathbf{L}\mathbf{F}\mathbf{V}_0 = \left(\frac{\omega}{k}\right)^2\mathbf{V}_0. \tag{3.3}$$

Equation (3.3) is an eigenproblem for $\mathbf{V}_0$ and ω^2/k^2 and can be solved numerically. Eight wave modes are obtained: $\pm k_{pf}$, $\pm k_{ps}$, $\pm k_s$ and 0 with multiplicity two, which correspond to the *fast p wave*, *slow p wave* and *shear wave* respectively. It is worthwhile to note that the wave modes depend on the frequency ω and the wave direction $(l_x,\ l_z)$.

With the wave modes, we deduce the phase velocities: $c_{pf} = \omega/\Re(k_{pf})$, $c_{ps} = \omega/\Re(k_{ps})$ and $c_s = \omega/\Re(k_s)$, satisfying $0 < c_{ps} < c_{pf}$ and $0 < c_s$. Simultaneously, the attenuations are also derived: $\alpha_{pf} = -\Im\mathrm{m}(k_{pf})$, $\alpha_{ps} = -\Im\mathrm{m}(k_{ps})$ and $\alpha_s = -\Im\mathrm{m}(k_s)$. As shown in (8), both the phase velocities and the attenuations of the Biot-LF and Biot-JKD are strictly increasing functions with respect to frequency. Theoretically, in the case that $f > f_c$ with f_c being the critical frequency, the *slow p wave* is highly damped, while the *fast p wave* and *the shear wave* are lightly damped; on the contrary, the phase velocities and the attenuations of the Biot-LF model and the Biot-JKD model are consistent when $f < f_c$. See Fig. 1.

4. Numerical methods for the poles and weights

In this section, we introduce *the best relative Chebyshev approximation* of the square-root function to determine the poles and weights in (2.33). To compare with the Stieltjes function (31) and the diffusive approximation (6; 8; 7; 22) for the convolution kernel, we also give a brief introduction of these two methods. For simplicity, the subscripts for indicating the principle directions are suppressed in the following statements.

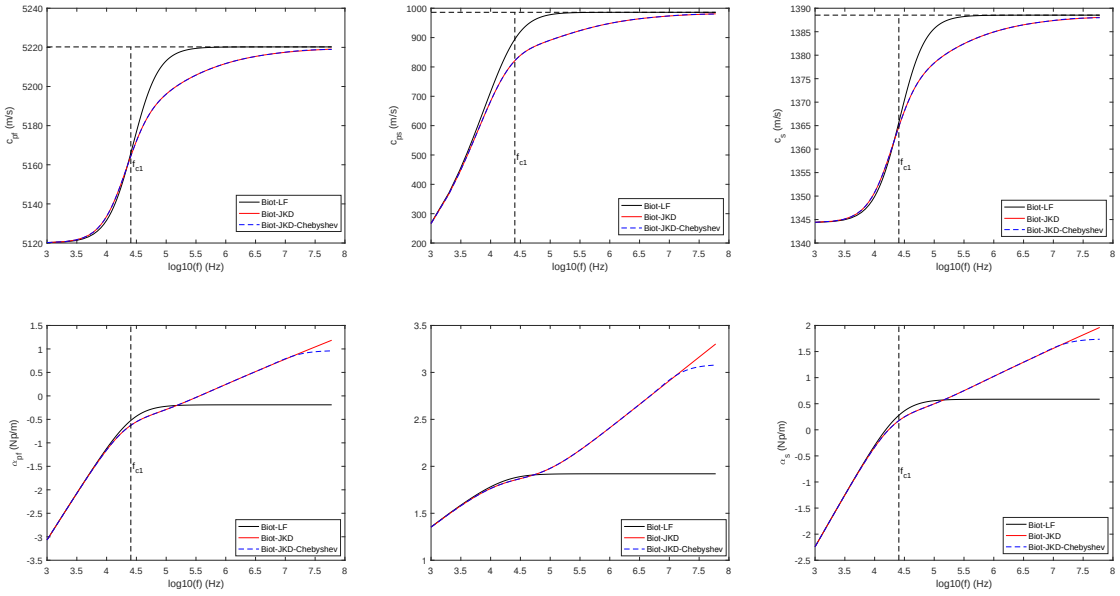

FIGURE 1. Dispersion results for for material J_3 with 15 poles and the wave direction $(1,0)$. Top: the phase velocities, bottom: the attenuations. Left to right: *the fast p wave*, *the slow p wave*, *the shear wave*.

4.1. **The best relative Chebyshev approximation for $\sqrt{x}$.** The function $\Phi_{q,q-1} \in \mathbb{R}_{q,q-1}, q \geq 1$, with $\mathbb{R}_{q,q-1}$ denoting the rational functions of degrees $(q, q-1)$, is *the best relative Chebyshev approximation* for $\sqrt{x}$ in $[a^2, b^2]$ if

$$\Phi_{q,q-1} = \arg \min_{g \in \mathbb{R}_{q,q-1}} \left\| \frac{g - \sqrt{x}}{\sqrt{x}} \right\|_{L^\infty[a^2,b^2]}.$$

Define

$$E_{q,q-1,[a^2,b^2]} := \left\| \frac{\Phi_{q,q-1} - \sqrt{x}}{\sqrt{x}} \right\|_{L^\infty[a^2,b^2]}.$$

Given two numbers a_0 and b_0 such that $0 < a_0 < b_0$, the sequences $\{a_j\}$ and $\{b_j\}$ are constructed recursively as follows

$$a_{j+1} = \sqrt{a_j b_j}, \quad b_{j+1} = \frac{1}{2}(a_j + b_j), \quad j \geq 0. \tag{4.1}$$

Clearly, $0 < a_j < b_j$, $j \geq 0$.

Lemma 4.1 ((9), Lemma 3.1)**.** *For $q \geq 1$ and (a_j, b_j) constructed according to (4.1), we have*

$$E_{q,q-1,[a_{j+1}^2, b_{j+1}^2]} = E_{2q,2q-1,[a_j^2,b_j^2]}.$$

The above Lemma provides a strategy to calculate the poles and weights recursively. Denote $r(x) := (x + a_j b_j)/2$ and $\xi := x/r^2(x)$, then ξ maps $[a_j^2, a_j b_j]$ and $[a_j b_j, b_j^2]$ onto $[1/b_{j+1}^2, 1/a_{j+1}^2]$ monotonously, and it holds that $\sqrt{x} = r(x)\sqrt{x/r^2(x)} = r(x)\sqrt{\xi}$. Suppose we have the following approximation

$$\sqrt{x} \backsimeq -\sum_{k=1}^{m} \frac{\omega_k}{x + p_k} + \omega_{m+1} x + \omega_{m+2} =: \Phi_{q,q-1}(x), \ m = 2^{q-1} - 1, \ q \geq 2, \tag{4.2}$$

where $p_k, \omega_k > 0$ are poles and weights of the rational function. As a result, one can derive

$$\Phi_{2q,2q-1,[a_j^2,b_j^2]}(x) = r(x)\Phi_{q,q-1,[1/b_{j+1}^2, 1/a_{j+1}^2]}(\xi) \in \mathbb{R}_{2q,2q-1}, \quad q \in \mathbb{Z}^+,$$

which provides an approximation for the interval $[a_j^2, b_j^2]$ with the same maximal relative error as $\Phi_{q,q-1}$ on the interval $[1/b_{j+1}^2, 1/a_{j+1}^2]$. Obviously, $\frac{r(x)}{\xi+p_k}$, $r(x)\xi$ and $r(x)$ are of degree $(3,2)$, $(1,1)$ and $(1,0)$, respectively, and thus one can determine the poles and weights easily and obtain all the poles and weights recursively as follows. The starting point of the recursive procedure is the *best constant approximating function*

$$\Phi_{0,0} = \frac{2ab}{a+b}, \quad E_{0,0} = \frac{b-a}{b+a}.$$

In particular, one has

$$\Phi_{1,0} = \frac{\sqrt{1-E_{0,0}^2}}{1+\sqrt{1-E_{0,0}^2}} \left(\frac{\Phi_{0,0}}{\sqrt{1-E_{0,0}^2}} + \sqrt{1-E_{0,0}^2}\, \frac{x}{\Phi_{0,0}} \right), \quad E_{1,0}^{-1} = \left(E_{0,0}^{-1} + \sqrt{E_{0,0}^{-2}-1} \right)^2,$$

and

$$E_{2q,2q-1}^{-1} = \left(E_{q,q-1}^{-1} + \sqrt{E_{q,q-1}^{-2}-1} \right)^2.$$

Theorem 4.1. *((9), Theorem 3.3) Let $[a,b] \subset R_+$, set $\ell = \sqrt{a/b}$ and $\eta(\ell) = \exp\left(\frac{\pi \mathbf{K}(\ell)}{\mathbf{K}'(\ell)}\right)$ with*

$$\mathbf{K}(\ell) := \int_0^\infty \frac{1}{\sqrt{(1+\theta^2)(1-\ell^2+\theta^2)}} d\theta, \quad \mathbf{K}'(\ell) := \int_0^\infty \frac{1}{\sqrt{(1+\theta^2)(\ell^2+\theta^2)}} d\theta.$$

Then

$$E_{q,q-1,[a,b]} \le 4\eta(\ell)^{-2q}, \quad \forall\ q \ge 1.$$

4.2. **Stieltjes function formulation.** Based on the fact that the tortuosity can be represented in terms of the Stieltjes function, the rational approximation was used to approximate the convolution kernel (31). Define the new function

$$D(s) := T(\omega) - \frac{\mathrm{i}\chi}{\omega} = \int_0^C \frac{d\sigma(t)}{1+st}, \quad C = \frac{4\alpha_\infty^2 \kappa^2}{\nu \phi^2 \Lambda^2}, \quad \chi := \frac{\eta\phi}{\rho_f \kappa}, \tag{4.3}$$

where $d\sigma$ is a probability measure, then D is a Stieltjes function and can be approximated as

$$D(s) = \int_0^C \frac{d\sigma(t)}{1+st} \approx \alpha_\infty + \sum_{\ell=1}^N \frac{r_\ell}{s-\theta_\ell}, \ s \in \mathbb{C} \backslash \left(-\infty, -\frac{1}{C} \right], \tag{4.4}$$

with the poles $\theta_\ell < 0$ and weights $r_\ell > 0$. The above approximation can be achieved by the two-sided residue interpolation method with interpolation points ω_ℓ:

$$s_\ell := -\mathrm{i}\omega_\ell, \quad u_\ell = s_\ell^{-1}, \quad v_\ell = D(s_\ell) - \alpha_\infty, \quad \ell = 1 \ldots N, \tag{4.5}$$

$$(S_1)_{pq} := \frac{s_p^* v_p^* - s_q v_q}{s_p^* - s_q} = \frac{-s_q D(s_q) + s_p^* D^*(s_p)}{s_p^* - s_q} - \alpha_\infty, \ p, q = 1 \ldots N, \tag{4.6}$$

$$(S_2)_{pq} := \frac{v_p^* - v_q}{s_q - s_p^*} = \frac{-D(s_q) + D^*(s_p)}{s_q - s_p^*}, \ p, q = 1 \ldots N. \tag{4.7}$$

where the superscript $*$ denotes the complex conjugation. In terms of the generalized eigenvalues/eigenvectors of S_1, S_2, i.e., $S_1 V = S_2 V \Phi$ with V being the matrix of generalized eigen vectors and Φ the diagonal matrix of generalized eigen values, the poles and weights are then given by

$$\theta_\ell = -\Phi(\ell,\ell), \quad r_\ell = C_+ V(:,\ell) V(:,\ell)^* C_+^*,$$

where

$$C_+ := (v_1, \cdots, v_N), \quad .$$

To handle the high condition number of the matrices involved, arbitrary precision code such as *Advanprix* should be used for implementing this algorithm.

4.3. **Diffusive approximation.** The shifted fractional derivative can be expressed as

$$(D+\lambda)^{1/2}q = e^{-\lambda t}D^{1/2}(e^{\lambda t}q) = \int_0^\infty \psi(x,z,t;y)dy \simeq \sum_{l=1}^{L} a_l\psi_l(x,z,t;y_l), \tag{4.8}$$

where

$$\psi(x,z,t;y) = \frac{2}{\pi}\int_0^t e^{-(t-\tau)y^2-\lambda(t-\tau)}\left[\lambda q(\tau) + \frac{\partial q}{\partial t}(\tau)\right]d\tau$$

is the auxiliary variable satisfying

$$\frac{\partial \psi}{\partial t} = -\left(y^2+\lambda\right)\psi + \frac{2}{\pi}\left[\lambda q + \frac{\partial q}{\partial t}\right]. \tag{4.9}$$

Replacing the convolution term with (4.8) and (4.9), one can obtain the Biot-DA model (8). Many methods have been used to determine the coefficients a_ℓ and y_ℓ. The modified Gauss-Laguerre quadrature with slowly convergence was used in (22). The optimization method was developed in (8), which was much more accurate than those obtained with Gaussian quadratures. Note that the viscous operator is

$$\widehat{F}^{JKD}(\omega) = \left(1 + \mathrm{i}\omega\frac{4\alpha_\infty^2\kappa^2\rho_f}{\eta\Lambda^2\phi^2}\right)^{1/2} = \frac{1}{\sqrt{\lambda}}\left(\lambda+\mathrm{i}\omega\right)^{1/2}.$$

Applying the Fourier transform to (4.8), one has the following approximation

$$\widehat{F}^{DA}(\omega) = \frac{\lambda+\mathrm{i}\omega}{\sqrt{\lambda}}\sum_{l=1}^{N}\frac{a_l}{y_\ell^2+\lambda+\mathrm{i}\omega}.$$

Clearly, one can establish the following objective function

$$\chi^2 = \sum_{k=1}^{K}\left|\frac{F^{DA}}{F^{JKD}} - 1\right|^2.$$

Now for any partition of the given frequency range $[\omega_{min},\ \omega_{max}]$, the optimization problem reads as

$$\min_{\bar{a}_\ell, y_\ell}\chi^2 = \min_{\bar{a}_\ell^2, y_\ell}\sum_{k=1}^{K}\left|\sum_{\ell=1}^{N}\bar{a}_\ell\frac{(\lambda+\mathrm{i}\omega_k)^{1/2}}{y_\ell^2+\lambda+\mathrm{i}\omega_k} - 1\right|^2, \quad y_\ell \le \omega_{max}, \quad \bar{a}_\ell^2 = a_\ell.$$

The values of K and N are crucial, which influence the accuracy of this method, see (8) for more details. In the above, the frequency range is set as $\omega_{min} = \omega_c/10, \omega_{max} = 10\omega_c$ with ω_c being the peak frequency of the selected Ricker wavelet. In the implementation, the above problem is solved by using the SolvOpt (19; 28) and the initial data for a_ℓ and y_ℓ are obtained by using modified Gauss-Jacobi quadratures and the sample points are chosen as

$$\omega_k = \omega_{min}\left(\frac{\omega_{max}}{\omega_{min}}\right)^{\frac{k-1}{K-1}}, \quad k = 1,\cdots,K.$$

5. Numerical method

5.1. **Space discretization.** Let Ω be the computational domain and Ω_h be a partition of Ω. For any element $K \in \Omega_h$, we define the approximation space consisting of piecewise polynomials

$$V_h^k = \{v : v|_K \in P^n(K), K \in \Omega_h\},$$

where $P^k(K)$ indicates the collection of polynomials of degree at most k on element K. The semi-discrete DG method for (2.33) is to find $\mathbf{Q}_h \in (V_h^k)^{8+2m}$, such that for all $K \in \Omega_h$ and $\boldsymbol{\varphi} \in (V_h^k)^{8+2m}$, it holds that

$$\frac{d}{dt}\int_K \mathbf{Q}_h\cdot\boldsymbol{\varphi}\,dxdz + \int_{\partial K}\mathcal{H}\left(\mathbf{Q}_h^{int},\mathbf{Q}_h^{ext}\right)\cdot\boldsymbol{\varphi}\,ds - \int_K \mathbf{F}(\mathbf{Q}_h)\cdot\nabla\boldsymbol{\varphi}\,dxdz = \int_K \mathbf{h}(\mathbf{Q}_h)\cdot\boldsymbol{\varphi}\,dxdz,$$

where $\mathbf{F}(\mathbf{Q}_h) = (\mathbf{A}\mathbf{Q}_h, \mathbf{B}\mathbf{Q}_h)$, $\mathbf{h}(\mathbf{Q}_h) = \mathbf{H}\mathbf{Q}_h$, $\mathbf{Q}^{int}$ and $\mathbf{Q}^{ext}$ are the traces of $\mathbf{Q}$ on ∂K calculated from the interior of K and the exterior adjacent K', and $\mathcal{H}$ is the numerical flux. In this work, the Lax-Friedrichs flux (local) is employed

$$\mathcal{H}(\mathbf{Q}_h^{int}, \mathbf{Q}_h^{ext}) = \frac{1}{2}\left[\mathbf{F}(\mathbf{Q}_h^{int}) \cdot \mathbf{n}_{\partial K} + \mathbf{F}(\mathbf{Q}_h^{ext}) \cdot \mathbf{n}_{\partial K} - \alpha_{\partial K}(\mathbf{Q}_h^{ext} - \mathbf{Q}_h^{int})\right],$$

where $\alpha_{\partial K}$ is an estimate of the biggest eigenvalue of Jacobian matrix in a neighborhood of ∂K, and $\mathbf{n}_{\partial K}$ is the unit outward normal of ∂K from K to K'.

5.2. **Operator splitting.** In the numerical implementation of (2.33), one of the difficulties is to handle the viscous dissipation term, which has its own decay timescale and may cause the poroelasticity system to be stiff. As shown in (8), the stability condition of the direct method requires

$$\Delta t' \leq \min\left(\Delta t, \ \frac{2}{R(\mathbf{H})}\right),$$

where $R(\mathbf{H})$ is the spectral radius of $\mathbf{H}$, and Δt depends on the left hand side of (2.33) and is determined by (13)

$$\Delta t = \frac{\mathrm{CFL}}{\max_{K\in\Omega_h} \|(c_1(K), c_3(K))\| \times perimeter(K)/|K|}$$

with $|K|$ being the area of the triangle element and $c_j(K), j = 1, 3$ the speeds of the waves. According to Theorem 2.2, we know

$$R(\mathbf{H}) > \max_{k=1,\cdots,m}\left\{p_k^1 + \lambda_1, p_k^3 + \lambda_3\right\}.$$

With highly dissipative fluids or large value of poles, the computational time step can be so small that makes the simulation highly inefficient.

Instead of solving the original system (2.33) directly, we apply the splitting method by splitting the original system into a homogeneous conservation law

$$\frac{\partial \mathbf{Q}}{\partial t} + \mathbf{A}\frac{\partial \mathbf{Q}}{\partial x} + \mathbf{B}\frac{\partial \mathbf{Q}}{\partial z} = 0, \qquad (\mathcal{Q}_1),$$

and an ordinary differential equation

$$\frac{\partial \mathbf{Q}}{\partial t} = \mathbf{H}\mathbf{Q} + \mathbf{S}, \qquad (\mathcal{Q}_2),$$

where $\mathcal{Q}_1$ and $\mathcal{Q}_2$ are the relevant operators. Then the subproblems can be solved by different solvers and thus to optimize the time step. In this work, the second-order Strang splitting method (21) is employed to solve $(\mathcal{Q}_1)$ and $(\mathcal{Q}_2)$ alternatively, and the algorithm is as follows:

- step 1: solve $\mathcal{Q}_2$ with $\Delta t/2$ and initial data $\mathbf{Q}^n$

$$\widetilde{\mathbf{Q}} = \mathcal{Q}_2\left(t_n, \frac{\Delta t}{2}\right)\mathbf{Q}^n,$$

- step 2: solve $\mathcal{Q}_1$ with Δt and initial data $\widetilde{\mathbf{Q}}$

$$\mathbf{Q}' = \mathcal{Q}_1\left(t_n, \Delta t\right)\widetilde{\mathbf{Q}},$$

- step 3: solve $\mathcal{Q}_2$ with $\Delta t/2$ and initial data $\mathbf{Q}'$

$$\mathbf{Q}^{n+1} = \mathcal{Q}_2\left(t_{n+1}, \frac{\Delta t}{2}\right)\mathbf{Q}'.$$

5.3. **Time discretization.** In the implementation, we apply a strong stability preserving high order (17) scheme for the time discretization. Such discretizations can be expressed as a convex combination of the forward Euler method, and thus they maintain strong stability properties in any semi-norm of the forward Euler step. Consider the following ODE system

$$\frac{d}{dt}\mathbf{Q} = \mathcal{L}(\mathbf{Q}).$$

Let $\{t^n\}_{n=0}^N$ be a partition of $[0, T]$, with uniform time step Δt, the third order total variation diminishing (TVD) Runge-Kutta method is given as follows:

$$\begin{aligned}\mathbf{Q}^{(1)} &= \mathbf{Q}^n + \Delta t\mathcal{L}(\mathbf{Q}^n, t^n),\\ \mathbf{Q}^{(2)} &= \frac{3}{4}\mathbf{Q}^n + \frac{1}{4}\mathbf{Q}^{(1)} + \frac{1}{4}\Delta t\mathcal{L}(\mathbf{Q}^{(1)}),\\ \mathbf{Q}^{n+1} &= \frac{1}{3}\mathbf{Q}^n + \frac{2}{3}\mathbf{Q}^{(2)} + \frac{2}{3}\Delta t\mathcal{L}(\mathbf{Q}^{(2)}).\end{aligned}$$

5.4. **Interface condition.** When we consider the heterogeneous media with a stationary interface, the following imperfect hydraulic contact condition (14) is needed

$$[\mathbf{v}] = 0, \quad [\mathbf{q}\cdot\mathbf{n}] = 0, \quad [p] = 0, \quad [\overline{\boldsymbol{\tau}}\,\mathbf{n}] = 0,$$

where $[\cdot]$ means the jump at the interface. The first condition indicates that the materials are connected at the interface; the second one states that all fluids entering the interface should exit the other side; the third one shows that the difference of the pressure across the interface is zero and the last one is a statement of the continuity of the stress.

6. Numerical results

In this section, numerical examples are presented to demonstrate the validation of the proposed numerical method. The properties of the materials used for the forthcoming examples are given in Table 1. The viscous characteristic lengths Λ_1 and Λ_3 are calculated by setting the Pride numbers $P_1 = P_3 = 0.5$. The poles and weights with frequency interval $[300, 1500]$ and $m = 7$ are used for all materials. In the implementation of numerics, without loss of generality, the principal directions of the material are assumed to coincide with the global coordinate axes.

		J_1	J_2	J_3	J_4
Basic	*properties*				
K_s	(Gpa)	40	36.66	40	40
ρ_s	(kg/m^3)	1815	2644	1815	1815
c_{11}	(Gpa)	39.4	19.652	39.4	39.4
c_{12}	(Gpa)	1.0	5.572	1.0	1.0
c_{13}	(Gpa)	5.8	5.572	5.8	5.8
c_{33}	(Gpa)	13.1	19.652	13.1	13.1
c_{55}	(Gpa)	3.0	7.04	3.0	3.0
ϕ		0.2	0.2	0.2	0.2
κ_1	$(10^{-15}m^2)$	600	360	600	100
κ_3	$(10^{-15}m^2)$	100	360	600	100
$\alpha_{\infty 1}$		2	2.4	2	3.6
$\alpha_{\infty 3}$		3.6	2.4	2	3.6
K_f	(Gpa)	2.5	2.2495	2.5	2.5
ρ_f	(kg/m^3)	1040	1000	1040	1040
η	$(10^{-3}kg/m.s)$	1	1	1	1
Λ_1	$(10^{-6}m)$	6.93	5.88	6.93	3.79
Λ_3	$(10^{-6}m)$	3.79	5.88	6.93	3.79

Table 1. Material properties

6.1. **Validation of the rational approximation.** As the first example, we aim to assess the performance of the best relative Chebyshev approximation of the square root function. For this purpose, we illustrate the relative error between $\sqrt{s+\lambda}$ and $\Phi(s+\lambda)$ in the right half complex plane with different poles and weights, where λ is given by (2.9). The considered materials are the transversely isotropic $J_4$with the critical frequencies $f_{cz} = 85$ kHz. The interest interval is $[300, 1500]$ which should contain the critical

frequencies and the frequency f_0 of the source function. To compare with the Stieltjes IRF and DA approximation, we show the results with different number of poles and weights in Fig. 2, from which we can see that the proposed approach approximates the kernel very well. In addition, we can see that the results by Chebyshev approximation are comparable to those by the Stieltjes IRF and are better than those by the DA method.

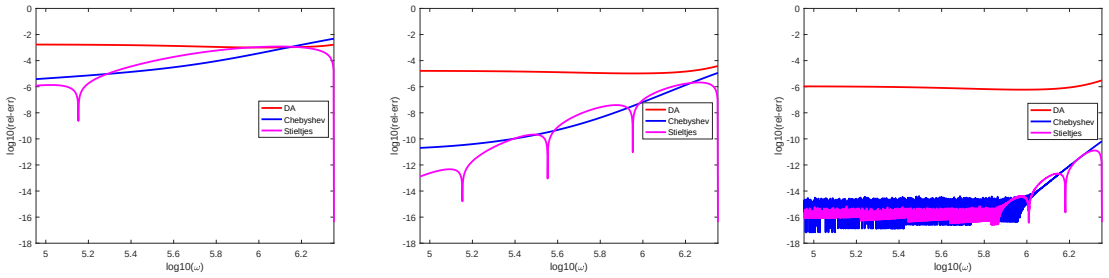

(A) N=3 (B) N=7 (C) N=15

FIGURE 2. Results comparison for different methods and different N.

6.2. **Homogeneous medium.** In this example, we demonstrate the phenomena of waves in poroelastic media by solving the approximated Biot-JKD equation (2.33) with the proposed DG method. The problem setup is that the homogeneous medium J_1 is excited by a source point acting only on τ_{13}. The source is located at the center of the medium and is expressed as

$$S = -g(t)h(x,z)/(\pi * r_0^2), \tag{6.1}$$

where

$$g(t) = \begin{cases} (1-2\pi^2 f_0^2(t-t_d)^2)\exp(-\pi^2 f_0^2(t-t_d)^2) & \text{if } 0 \le t \le 2t_d, \\ 0 & \text{otherwise,} \end{cases}$$

with the peak frequency $f_0 = 200$ kHz and the time delay $t_d = 1/f_0$ is a Ricker wavelet, and

$$h(x,z) = \begin{cases} \frac{1}{\pi\Sigma^2}\exp\left(-\frac{x^2+z^2}{\Sigma^2}\right) & \text{if } \ 0 \le x^2+z^2 \le r_0^2, \\ 0 & \text{otherwise,} \end{cases}$$

with radius $r_0 = 6.56\times10^{-3}$ m and $\Sigma = 3.28\times10^{-3}$ m is a truncated Gaussian function. The computational domain is $\Omega = [-0.15,\ 0.15]^2\ m^2$, which includes about 10 *fast p waves* and is partitioned with 247772 triangle elements. The total simulation time is 2.72×10^{-5} s, including about 6 periods of the *fast p wave*. The initial condition is set to be zero and the CFL number is set to be 0.3. No special care is paid to the boundary condition since the waves will not reach the boundary during the simulation. For comparison, we solve the Biot-DA model (8), where the relevant weights and abscissae are determined by solving a nonlinear optimization problem.

The snapshot of the pressure at the final time is presented in Fig. 3 (a). Three waves of *the fast p wave*, *the slow p wave* and *the shear wave* are observed, which are analogous to the results shown in (31; 8). Meanwhile, we can see from Fig. 3 (b) and (c) that the pressure at $z = -0.02$ m of the rational approximated Biot-JKD model and the Biot-DA model show excellent agreement.

6.3. **Heterogeneous media with horizontal interfaces .** In this example, heterogeneous media with horizontal interfaces are considered to illustrate the ability of the proposed method for complex geometry. We start with the the case that J_1 and J_2 separated by $z = 0$ m and then replace the interface by $z = \pm0.02$ m, see Fig. 4 for the illustration. The computational domain is $[-0.15,\ 0.15]^2\, m^2$, which is discretized into 156330 and 223948 nonuniform triangle elements by refining the meshes around the interfaces respectively. The source point (6.1) located at the center of the domain is used to emit cylindrical waves and is only applied to τ_{13}. The initial condition is set to be zero and the boundary condition is chosen to be outflow

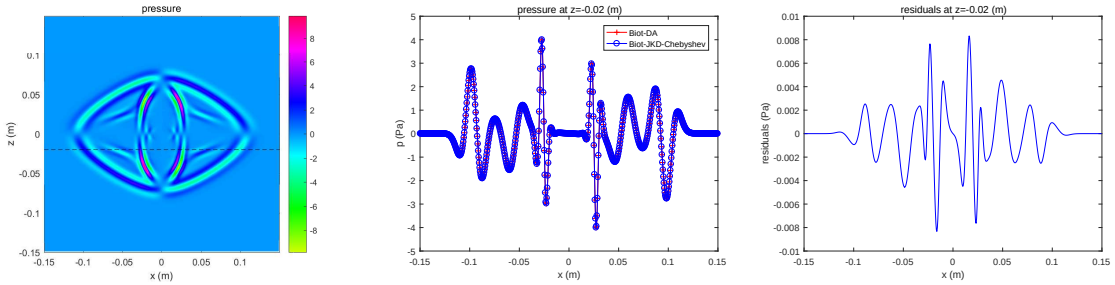

(A) (B) (C)

FIGURE 3. Results of the pressure for example 6.2. (a) Snapshot at the finial time, the dash line denotes z=-0.02 m, (b) pressure along the line z=-0.02 m, (c) residuals at z=-0.02 m between the Biot-DA model and Biot-JKD model with the rational approximation.

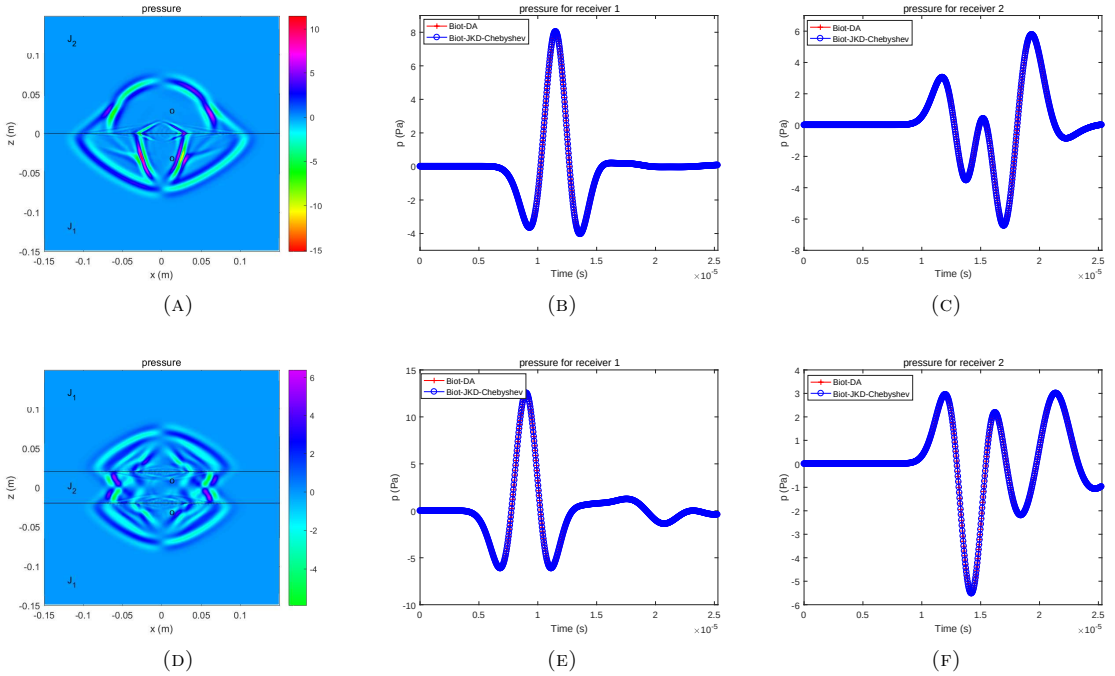

(A) (B) (C)

(D) (E) (F)

FIGURE 4. Results of the pressure for Example 6.3, the horizontal real lines in (a) and (d) denote the interfaces, and the ∘ represents the locations of the receivers. Top: results for the one line interface case, (a) snapshot of the pressure at the finial time, (b) time histories of the receiver (0.01,0.02) m, (c) time histories of the receiver (0.01,-0.02) m. Bottom: results for the two line interfaces case, (d) snapshot of the pressure at the finial time, (e) time histories of the receiver (0.01,0.01) m, (f) time histories of the receiver (0.01,-0.03) m.

boundary condition. The total simulation time is $2.53 \times 10^{-5}s$, the CFL number is set to be 0.3 and the componentwise limiter (13) with $\mathcal{M} = 50$ and $\nu = 1.5$ is used in this test.

The snapshots of the pressure at the final time are presented in Fig. 4 (a) and (d) for the two cases respectively. The reflected and transmitted waves are observed, enriching and complicating the structures of the solution. In addition to the time-snapshot, we also record the time evolution of the pressure at two receivers situated at $(0.01, \pm 0.02)$ m for the one interface case, and (0.01,0.01) m and (0.01,-0.03) m for

the two interfaces case respectively. Again we use the RKDG method to solve the Biot-DA model as the reference solution. The relevant results show that the solutions from the two methods are indistinguishable.

6.4. **Heterogeneous media with circular interfaces .** As the last example, we consider a more complex geometry example that the heterogeneous media J_3 and J_4 are separated by circular interfaces. Two cases of one circular interface $x^2 + z^2 \leq 0.05$ and two circular interfaces $x^2 + z^2 \leq 0.05, x^2 + z^2 \leq 0.03$ are considered, see Fig. 5 for the illustration. The computational domain is $[-0.15,\ 0.15]^2\, m^2$, which is divided into 132896 nonuniform triangle elements by refining the meshes around the interfaces. The system is excited by the source point (6.1), which is located at the center of the domain and is only employed to τ_{13}. The initial condition is set to be zero and the boundary condition is chosen to be outflow boundary condition. The the total simulation time is $2.53 \times 10^{-5} s$ and the CFL number is set to be 0.3. In the implement of simulation, the componentwise limiter with $\mathcal{M} = 50$ and $\nu = 1.5$ is used in this test.

The receivers of $(0.01, \pm 0.025)$ m for the one interface case and $(0.01, 0.025)$ m and $(0.01, 0.04)$ m for the two interfaces case are chosen to record the time evolution of the pressure. We present the snapshot of the pressure at the final time and the time histories in Fig. 5, from which we can observe that the solutions given by the rational approximated Biot-JKD model and Biot-DA model in the complex geometry are consistent.

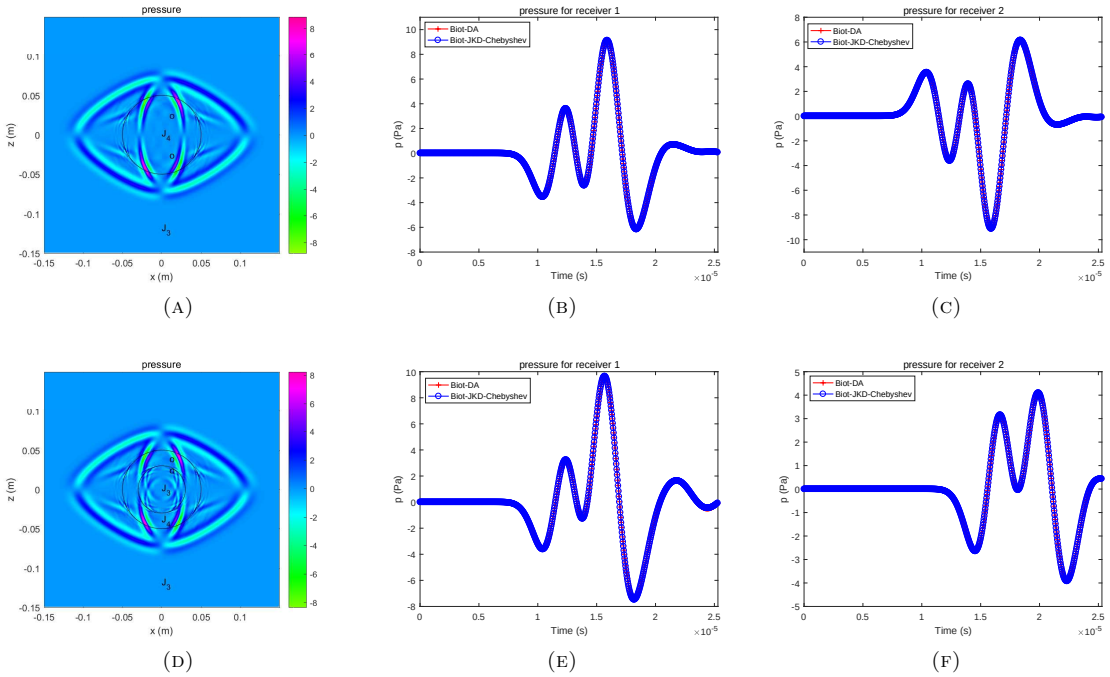

FIGURE 5. Results of the pressure for example 6.4, the interfaces are mapped with the circular real lines in (a) and (d), and the locations of the receivers are marked with ∘. Top: results for the one line interface case, (a) snapshot of the pressure at the finial time, (b) time histories of the receiver (0.01,0.025) m, (c) time histories of the receiver (0.01,-0.025) m. Bottom: results for the two line interfaces case, (d) snapshot of the pressure at the finial time, (e) time histories of the receiver (0.01,0.025) m, (f) time histories of the receiver (0.01,0.04) m.

7. Conclusion and future works

In this work, we have derived an approximate Biot-JKD model and developed a DG method with operator splitting to investigate wave propagation in orthotropic poroelastic media. The Biot-JKD model,

containing the temporal convolution and stiff property, is challenging to be implemented numerically. To avoid storage and integration of the entire variable histories, we propose a fast algorithm based on the rational approximation in which the required poles and weights are calculated with high accuracy by using the technique of *the best relative Chebyshev approximation* of the square-root function. For completeness, we also present in the paper two competitive existing methods for computing the poles and weights. One is based on the Stieltjes function (SF) formulation and the other on the diffusion approximation (DA). In comparison with SF, the new method does not require any arbitrary precision arithmetic system for computing the poles and weights; this is a big advantage. However, the SF approach is able to handle more general cases where the memory kernels are not of square-root function type. Indeed, the SF approach only require a finite set of interpolation points without demanding the kernel to be in any specific functional form. For the JKD kernel, we do see the advantage of the new method over SF.

By splitting the temporal convolution into a sequence of continuum local ODEs with the auxiliary variables, we derive a more tractable model with finite memory variables and zero components of the flux for the auxiliary variables. The RKDG method with the Strang splitting method is used to solve the approximated Biot-JKD equation. Both the homogeneous and heterogeneous cases are considered.

In the future, we will extend the idea of this paper to some other dissipative problems whose governing equations contain fractional derivative with order 1/2. We will also consider the inverse problem of the multiparameter full waveform inversion in poroelastic medium.

Acknowledgments

The work of J. Xie is partially supported by a NSFC Grant (No. 12171274) and a NSFC Grant (No. 12171465). The work of M. Li is partially supported by a NSFC Grant (No. 11871139). MYO's work was partial sponsored by US NSF Grants DMS-1413039 and DMS-1821857.

Appendix A. The proof of Theorem 2.1

Proof. To begin with, we prove that the energy function $\mathcal{E}$ is positive definite. Clearly, both $\mathcal{E}_2$ and $\mathcal{E}_3$ are positive definite. Since $\det(\mathcal{M}_j) > 0, \rho > 0, \mu_j > 0$, we know that $\mathcal{E}_1$ is positive definite.

In the following, we prove that (2.18) holds. Multiplying (2.6) with $\mathbf{v}^T$ and integrating on $\mathbb{R}$, we obtain

$$0 = \int_{\mathbb{R}^2} \left(\rho \mathbf{v}^T \frac{\partial \mathbf{v}}{\partial t} + \rho_f \mathbf{v}^T \frac{\partial \mathbf{q}}{\partial t} - \mathbf{v}^T \nabla \cdot \overline{\boldsymbol{\tau}} \right) dxdz.$$

By the Fourier transform, we have

$$0 = \int_{\mathbb{R}^2} \left(\rho \hat{\mathbf{v}}^T s \hat{\mathbf{v}}^T + \rho_f \hat{\mathbf{v}}^T s \hat{\mathbf{q}} - \hat{\mathbf{v}}^T \nabla \cdot \hat{\overline{\boldsymbol{\tau}}} \right) dxdz. \tag{A.1}$$

Integrating by part and using $\mathbf{v} = \partial_t \mathbf{u}$, $\epsilon_{ij} = (\partial_i u_j + \partial_j u_i)/2$, it is easy to check that

$$-\int_{\mathbb{R}^2} \hat{\mathbf{v}}^T \nabla \cdot \hat{\overline{\boldsymbol{\tau}}} dxdz = \int_{\mathbb{R}^2} \hat{\boldsymbol{\tau}}^T s \hat{\boldsymbol{\epsilon}} dxdz,$$

which together with (2.4) leads to

$$-\int_{\mathbb{R}^2} \hat{\mathbf{v}}^T \nabla \cdot \hat{\overline{\boldsymbol{\tau}}} dxdz = \int_{\mathbb{R}^2} \hat{\boldsymbol{\tau}}^T \mathbf{C}^{-1} s \hat{\boldsymbol{\tau}} + \hat{\boldsymbol{\tau}}^T \mathbf{C}^{-1} \boldsymbol{\beta} sp \, dxdz.$$

With the above equation, (A.1) is reformulated as

$$0 = \int_{\mathbb{R}^2} \left(\rho \hat{\mathbf{v}}^T s \hat{\mathbf{v}}^T + \rho_f \hat{\mathbf{v}}^T s \hat{\mathbf{q}} + \hat{\boldsymbol{\tau}}^T \mathbf{C}^{-1} s \hat{\boldsymbol{\tau}} + \hat{\boldsymbol{\tau}}^T \mathbf{C}^{-1} \boldsymbol{\beta} sp \right) dxdz. \tag{A.2}$$

Multiplying (2.15) with $\mathbf{q}^T$ and integrating on $\mathbb{R}$ gives

$$0 = \int_{\mathbb{R}^2} \left[\rho_f \mathbf{q}^T \frac{\partial \mathbf{v}}{\partial t} + \mathbf{q}^T \mathrm{diag}(\mu_j) \frac{\partial \mathbf{q}}{\partial t} + \mathbf{q}^T \nabla p + \mathbf{q}^T \mathrm{diag} \left(\vartheta_j \left(\partial_t + \lambda_j \right)^{1/2} \right) \mathbf{q} \right] dxdz, \ j = 1, 3.$$

Again by the Fourier transform, we have

$$0 = \int_{\mathbb{R}^2} \left[\rho_f \hat{\mathbf{q}}^T s \hat{\mathbf{v}} + \hat{\mathbf{q}}^T \mathrm{diag}(\mu_j) s \hat{\mathbf{q}} + \hat{\mathbf{q}}^T \nabla \hat{p} + \hat{\mathbf{q}}^T \mathrm{diag} \left(\vartheta_j \left(s + \lambda_j \right)^{1/2} \right) \hat{\mathbf{q}} \right] dxdz, \tag{A.3}$$

Integrating by part and using $\mathbf{q}=\partial_t\mathbf{w},\ \zeta=-\nabla\cdot\mathbf{w}$ as well as (2.4)-(2.5), we see

$$\begin{aligned}\int_{\mathbb{R}^2}\hat{\mathbf{q}}^T\nabla\hat{p}\,dxdz&=-\int_{\mathbb{R}^2}p\nabla\cdot\hat{\mathbf{q}}\,dxdz=\int_{\mathbb{R}^2}\hat{p}s\hat{\zeta}\,dxdz=\int_{\mathbb{R}^2}\hat{p}s\left(\frac{1}{M}\hat{p}+\boldsymbol{\beta}^T\hat{\boldsymbol{\epsilon}}\right)dxdz\\&=\int_{\mathbb{R}^2}\frac{1}{M}\hat{p}s\hat{p}\,dxdz+\int_{\mathbb{R}^2}\left(\hat{p}s\boldsymbol{\beta}^T\mathbf{C}^{-1}\hat{\boldsymbol{\tau}}+\hat{p}s\hat{\boldsymbol{\beta}}^T\mathbf{C}^{-1}\boldsymbol{\beta}\hat{p}\right)dxdz,\end{aligned}$$

which together with (A.3) implies

$$\begin{aligned}&-\int_{\mathbb{R}^2}\hat{\mathbf{q}}^T\mathrm{diag}\left(\vartheta_j\left(s+\lambda_j\right)^{1/2}\right)\hat{\mathbf{q}}\,dxdz\\&=\int_{\mathbb{R}^2}\left[\rho_f\hat{\mathbf{q}}^Ts\hat{\mathbf{v}}+\hat{\mathbf{q}}^T\mathrm{diag}(\mu_j)s\hat{\mathbf{q}}+\frac{1}{M}\hat{p}s\hat{p}+\boldsymbol{\beta}^T\mathbf{C}^{-1}\hat{\boldsymbol{\tau}}s\hat{p}+\boldsymbol{\beta}^T\mathbf{C}^{-1}\boldsymbol{\beta}\hat{p}s\hat{p}\right]dxdz.\end{aligned}\tag{A.4}$$

Summing up (A.2) and (A.4), and combining $\mathcal{E}_1$ and $\mathcal{E}_2$, we derive

$$\mathcal{L}\left[\frac{d(\mathcal{E}_1+\mathcal{E}_2)}{dt}\right]=-\int_{\mathbb{R}^2}\hat{\mathbf{q}}^T\mathrm{diag}\left(\vartheta_j\left(s+\lambda_j\right)^{1/2}\right)\hat{\mathbf{q}}\,dxdz=-\frac{2}{\pi}\int_{\mathbb{R}^2}\int_0^\infty\hat{\mathbf{q}}^T\mathrm{diag}\left(\vartheta_j\right)\boldsymbol{\psi}\,dydxdz,\tag{A.5}$$

where (2.16) is used and $\boldsymbol{\psi}=(\psi_1,\ \psi_3)^T$.

Multiplying (2.17) with $(\boldsymbol{\psi}-\mathbf{q})^T$ and using the Fourier transform, we obtain

$$\hat{\mathbf{q}}^T\mathrm{diag}\left(y^2+2\lambda_j\right)\hat{\boldsymbol{\psi}}=\left(\hat{\boldsymbol{\psi}}-\hat{\mathbf{q}}\right)^Ts\left(\hat{\boldsymbol{\psi}}-\hat{\mathbf{q}}\right)+\hat{\boldsymbol{\psi}}^T\mathrm{diag}\left(y^2+\lambda_j\right)\hat{\boldsymbol{\psi}}+\hat{\mathbf{q}}^T\mathrm{diag}\left(\lambda_j\right)\hat{\mathbf{q}},$$

which indicates

$$\begin{aligned}\hat{\mathbf{q}}^T\mathrm{diag}\left(\vartheta_j\right)\hat{\boldsymbol{\psi}}=&\left(\hat{\boldsymbol{\psi}}-\hat{\mathbf{q}}\right)^T\mathrm{diag}\left(\frac{\vartheta_j}{y^2+2\lambda_j}\right)s\left(\hat{\boldsymbol{\psi}}-\hat{\mathbf{q}}\right)\\&+\hat{\boldsymbol{\psi}}^T\mathrm{diag}\left(\frac{y^2+\lambda_j}{y^2+2\lambda_j}\vartheta_j\right)\hat{\boldsymbol{\psi}}+\hat{\mathbf{q}}^T\mathrm{diag}\left(\frac{\lambda_j\vartheta_j}{y^2+2\lambda_j}\right)\hat{\mathbf{q}},\ j=1,3.\end{aligned}$$

Combining the above equations and $\mathcal{E}_3$, we arrive at

$$\mathcal{L}\left[\frac{d\mathcal{E}}{dt}\right]=-\frac{2}{\pi}\int_{\mathbb{R}^2}\int_0^\infty\left[\hat{\boldsymbol{\psi}}^T\mathrm{diag}\left(\frac{y^2+\lambda_j}{y^2+2\lambda_j}\vartheta_j\right)\hat{\boldsymbol{\psi}}+\hat{\mathbf{q}}^T\mathrm{diag}\left(\frac{\lambda_j\vartheta_j}{y^2+2\lambda_j}\right)\hat{\mathbf{q}}\right]dydxdz\le 0.$$

Translating to time domain completes the proof.

□

Appendix B. The proof of Theorem 2.2

Proof. Let $\mathbf{Q}'=(v_x,\ q_x,\ H_1^x,\cdots,H_m^x,\ v_z,\ q_z,\ H_1^z,\cdots,\ H_m^z,\ \tau_{xx},\ \tau_{zz},\ \tau_{xz},\ p)^T$, then the matrix of the diffusive part is

$$\widetilde{\mathbf{H}}=\begin{bmatrix}\widetilde{\mathbf{H}}_1&\mathbf{0}&\mathbf{0}\\\mathbf{0}&\widetilde{\mathbf{H}}_3&\mathbf{0}\\\mathbf{0}&\mathbf{0}&\mathbf{0}_{4\times4}\end{bmatrix},$$

where

$$\widetilde{\mathbf{H}}_j=\begin{bmatrix}0&\frac{\rho_f\vartheta_j\left(\lambda_j\omega_{m+1}^j+\omega_{m+2}^j\right)}{\gamma_j}&-\frac{\rho_f\vartheta_j\omega_1^j}{\gamma_j}&-\frac{\rho_f\vartheta_j\omega_2^j}{\gamma_j}&\cdots&-\frac{\rho_f\vartheta_j\omega_m^j}{\gamma_j}\\0&-\frac{\rho\vartheta_j\left(\lambda_j\omega_{m+1}^j+\omega_{m+2}^j\right)}{\gamma_j}&\frac{\rho\vartheta_j\omega_1^j}{\gamma_j}&\frac{\rho\vartheta_j\omega_2^j}{\gamma_j}&\cdots&\frac{\rho\vartheta_j\omega_m^j}{\gamma_j}\\0&1&p_1^j+\lambda_j&0&\cdots&0\\0&1&0&p_2^j+\lambda_j&\cdots&0\\\vdots&\vdots&\vdots&\vdots&\ddots&\vdots\\0&1&0&0&0&p_m^j+\lambda_j\end{bmatrix},\quad j=1,3.$$

Clearly, the matrix $\mathbf{H}$ is similar to $\widetilde{\mathbf{H}}$. According to

$$\det\left(\tilde{\lambda}\mathrm{I}-\widetilde{\mathbf{H}}\right)=0,$$

we derive

$$\tilde{\lambda}^4\cdot\det\left(\tilde{\lambda}\mathrm{I}-\widetilde{\mathbf{H}}_1\right)\cdot\det\left(\tilde{\lambda}\mathrm{I}-\widetilde{\mathbf{H}}_3\right)=0.$$

By straightforward computing, we have

$$\begin{aligned}&\mathscr{P}(\tilde{\lambda}) := \det\left(\tilde{\lambda}\mathrm{I} - \widetilde{\mathbf{H}}_1\right)\\ &= \tilde{\lambda}\left[\left(\tilde{\lambda} - \frac{\rho\vartheta_1\left(\lambda_1\omega_{m+1}^1 + \omega_{m+2}^1\right)}{\gamma_1}\right)\prod_{k=1\cdots m}\left(\tilde{\lambda} - p_k^1 - \lambda_1\right) - \frac{\rho\vartheta_1}{\gamma_1}\sum_{k=1}^{m}\omega_k^1\prod_{\ell=1\cdots m,\ell\neq k}\left(\tilde{\lambda} - p_\ell^1 - \lambda_1\right)\right].\end{aligned}$$

Consequently, we know zero with multiplicity 1 is an eigenvalue of $\mathscr{P}(\tilde{\lambda})$. In addition, we obtain

$$\mathscr{P}(p_k^1 + \lambda_1) = -\left(p_k^1 + \lambda_1\right)\cdot\frac{\rho\vartheta_1}{\gamma_1}\omega_k^1\prod_{\ell=1\cdots m,\ell\neq k}\left(p_k^1 - p_\ell^1\right),$$

which together with $p_1^1 < p_2^1 \cdots < p_m^1$ and $m = 2^q - 1$ gives

$$\mathrm{sign}\mathscr{P}(p_k^1 + \lambda_1) = -\mathrm{sign}\mathscr{P}(p_{k+1}^1 + \lambda_1), \quad k = 1, \cdots m-1.$$

Particularly, we can check that

$$\mathscr{P}(0) = 0,\ \lim_{\tilde{\lambda}\to 0^+}\mathscr{P}(\tilde{\lambda}) > 0,\ \mathscr{P}(p_1^1 + \lambda_1) < 0,\ \mathscr{P}(p_m^1 + \lambda_1) < 0,\ \lim_{\tilde{\lambda}\to+\infty}\mathscr{P}(\tilde{\lambda}) > 0.$$

Thus we infer that there exist eigenvalues $\tilde{\lambda}_1$ in $(0, p_1^1 + \lambda_1)$ and $\tilde{\lambda}_{m+1}$ in $(p_m^1 + \lambda_1, +\infty)$. Together the above discussions, we know that the non-zero eigenvalues of $\widetilde{\mathbf{H}}_1$ satisfy

$$0 < \tilde{\lambda}_1^1 < p_1^1 + \lambda_1 < \cdots < \tilde{\lambda}_m^1 < p_m^1 + \lambda_1 < \tilde{\lambda}_{m+1}^1.$$

By repeated application, we can obtain the non-zero eigenvalues of $\widetilde{\mathbf{H}}_3$ satisfy

$$0 < \tilde{\lambda}_1^3 < p_1^3 + \lambda_3 < \cdots < \tilde{\lambda}_m^3 < p_m^3 + \lambda_3 < \tilde{\lambda}_{m+1}^3.$$

Recalling that $\widetilde{\mathbf{H}}$ is similar to $\mathbf{H}$, we finish the proof. □

References

[1] M. Avellaneda, S. Torquato, Rigorous link between fluid permeability, electrical conductivity, and relaxation times for transport in porous media, Phys. Fluids. A 3 (11) (1991) , pp. 2529 -2540.

[2] M. A. Biot, Theory of propagation of elastic waves in a fluid-saturated porous solid. I. Lowfrequency range, J. Acoust. Soc. Amer., 28 (1956), pp. 168-178.

[3] M. A. Biot, Theory of propagation of elastic waves in a fluid-saturated porous solid. II. Higher frequency range, J. Acoust. Soc. Amer., 28 (1956), pp. 179-191.

[4] M. A. Biot, Mechanics of deformation and acoustic propagation in porous media, J. Appl. Phys., 33 (1962), pp. 1482-1498.

[5] Y. Chen, Y. Luo, M. Feng, Analysis of a discontinuous Galerkin method for the Biot's consolidation probelm, Appl. Math. Comput., 219 (2013), pp. 9043-9056.

[6] E. Blanc, G. Chiavassa, B. Lombard, Biot-JKD model: simulation of 1D transient poroelastic waves with fractional derivatives, J. Comput. Phys., 237 (2013), pp. 1-20.

[7] E. Blanc, G. Chiavassa, B. Lombard, A time-domain numerical modeling of two-dimensional wave propagation in porous media with frequency-dependent dynamic permeability, J. Acoust. Soc. Amer., 134 (6) (2013), pp. 4610-4623.

[8] E. Blanc, G. Chiavassa, B. Lombard, Wave simulation in 2D heterogeneous transversely isotropic porous media with fractional attenuation: a Cartesian grid approach, J. Comput. Phys., 275 (2014), pp. 118-142.

[9] D. Braess, W. Hackbusch, On the efficient computation of high-dimensional integrals and the approximation by exponential sums, in: Multiscale, Nonlinear and Adaptive Approximation, Springer, 2009, pp. 39-74.

[10] J. Carcione, Wave propagation in anisotropic, saturated porous media: Plane-wave theory and numerical simulation, J. Acoust. Soc. Amer., 99 (1996), pp. 2655-2666.

[11] J. Carcione, C. Morency, J. Santos, Computational poroelasticity: A review, Geophys., 75 (2010), pp. 75A229-75A243.

[12] G. Chiavassa, B. Lombard, Time domain numerical modeling of wave propagation in 2D hetergeneous porous media, J. Comput. Phys., 230 (2011), pp. 1059-1080.
[13] B. Cockburn, C.-W. Shu, The Runge-Kutta discontinuous Galerkin method for conservation laws V: Multidimensional systems, J. Comput. Phys., 141 (1998), pp. 199-224.
[14] H. Deresiewicz, R. Skalak, On uniqueness in dynamic poroelasticity, Bulletin of the Seismological Society of America, 53 (1963), pp. 783-788.
[15] N. Dudley Ward, T. Lähivaara, S. Eveson, A discontinuous Galerkin methd for poroelastic wave propagation: the two-dimensional case, J. Comput. Phys., 350 (2017), pp. 690-727.
[16] S. Garg, A. Nayfeh, A. Good, Compression waves in fluid-saturated elastic porous media, J. Appl. Phys., 45 (1974), pp. 1968-1974.
[17] S. Gottlieb, C.-W. Shu, E. Tadmor, Strong stability preserving high order time discretization methods, SIAM Review 43 (2001), pp. 89-112.
[18] D. Johnson, J. Koplik, R. Dashen, Theory of dynamic permeability and tortuosity in fluid-saturated porous media, J. Fluid Mech., 176 (1987), pp. 379-402.
[19] F. Kappel, A. Kuntsevich, An implementation of Shors r-algorithm, Comput. Optim. Appl., 15(2) (2000) 193205.
[20] G. Lemoine, M. Y. Ou, R. LeVeque, High-resolution finite volume modeling of wave propagation in orthotropic poroelastic media, SIAM J. Sci. Comput., 35 (2013), pp. B176-B206.
[21] R. LeVeque, Finite Volume Methods for Hyperbolic Problems, Cambridge University Press, Cambridge, 2002.
[22] J. Lu, A. Hanyga, Wave field simulation for heterogeneous porous media with singular memory drag force, J. Comput. Phys., 208 (2) (2005), pp. 651-674.
[23] Y. Masson, S. Pride, Finite-difference modeling of Biot's poroelastic equations across all frequencies, Geophys., 75 (2) (2010), pp. N33-N44.
[24] M. Y. Ou, On reconstruction of dynamic permeability and tortuosity from data at distinct frequencies, Inverse Problems, 30 (2014), 095002.
[25] M. Y. Ou, Hugo Woerdeman, On the augmented Biot-JKD equations with Pole-Residue representation of the dynamic tortuosity, Operator Theory: Advances and Applications, Vol. 272, pp. 341-362, Springer Nature, 2019.
[26] S. Pride, F. Morgan, A. Gangi, Drag forces of porous-medium acoustics, Phys. Rev. B 47 (1993), pp. 4964-4978.
[27] J. de la Puente, M. Dumbser, M. Käser, H. Igel, Discontinuous Galerkin methods for wave propagation in poroelastic media, Geophys., 73 (2008), pp. T77-T97.
[28] N. Shor, Minimization Methods for Non-Differentiable Functions, Springer Ser. Comput. Math., vol.3, Springer-Verlag, Berlin, 1985.
[29] R. Sidler, J. Carcione, K. Holliger, A pseudo-spectral method for the simulation of poro-elastic seismeic wave propagation in 2D polar coordinates using domain decompsion, J. Comput. Phys., 235 (2013), pp. 846-864.
[30] T. Sun, J. Wang, C. Zheng, Fast evaluation of arificial boundary conditions for advection diffusion equations, SIAM J. Numer. Anal., 58 (2020), pp. 3530-3557.
[31] J. Xie, M.Y. Ou, L. Xu, A discontinuous Galerkin method for wave propagation in orthotropic poroelastic media with memory terms, J. Comput. Phys., 397 (2019), 108865.
[32] L. Zhang, L. Xu, T. Yin, An Accurate HyperSingular Boundary Integral Equation Method for Dynamic Poroelasticity in Two Dimensions, SIAM J. Sci. Comput., (43) 2021, pp. B784-B810
[33] Y. Zhang, J. Gao, W. Han, Y. He, A discontinuous Galerkin method for seismic wave propagation in coupled elastic and poroelastic media, Geophys. Prospect., 67 (2019), pp. 1392-1403.

Department of Mathematical Sciences, Tsinghua University, Beijing 10084, China
Email address: xiejiangming@mail.tsinghua.edu.cn

School of Mathematical Science, University of Electronic Science and Technology of China, Chengdu, Sichuan, 611731, P.R. China
Email address: limj@uestc.edu.cn

Department of Mathematical Sciences, University of Delaware, 408 Ewing Hall, Newark, Delaware 19716 USA
Email address: mou@udel.edu